Science Arts & Métiers (SAM)

is an open access repository that collects the work of Arts et Métiers ParisTech researchers and makes it freely available over the web where possible.

This is an author-deposited version published in: https://sam.ensam.eu
Handle ID: .http://hdl.handle.net/10985/8650

To cite this version :

Yann DUPLESSIS KERGOMARD, Frédéric DAU, Ivan IORDANOFF - Implementation of a Discrete Element Method for the space-time modeling of loading in the case of a soft shock: qualitative approach - Journal of Computations & Modelling - Vol. vol.1, n°2, p.39-72 - 2011

Any correspondence concerning this service should be sent to the repository Administrator : archiveouverte@ensam.eu

Arts et Métiers Institute of Technology

Journal of Computations & Modelling, vol.1, no.2, 2011, 39-72
ISSN: 1792-7625 (print), 1792-8850 (online)
International Scientific Press, 2011

Implementation of a Discrete Element Method for the space-time modeling of loading in the case of a soft shock: qualitative approach

Y. Duplessis Kergomard[1], F. Dau[2] and I. Iordanoff[3]

Abstract

The aim of this study is to modelize the space-time loading induced on a target by a deformable impactor, in the case of a "soft" shock. The originality of this work resides in the use of discrete elements to model the behaviour of the impactor, where large displacements and deformations can occur. A qualitative analysis is then developed to describe the changes in load applied to the target, as a function of the parameters relevant to such a shock.

Keywords: Soft shock, impactor, discrete elements

[1] Arts et Métiers ParisTech, Laboratoire LAMEFIP, Esplanade des arts et métiers, 33405 Talence cédex - France, e-mail: dkyznn@hotmail.com
[2] Arts et Métiers ParisTech, Laboratoire LAMEFIP, Esplanade des arts et métiers, 33405 Talence cédex - France, e-mail: frederic.dau@ensam.eu
[3] Arts et Métiers ParisTech, Laboratoire LAMEFIP, Esplanade des arts et métiers, 33405 Talence cédex - France, e-mail: ivan.iordanoff@ensam.eu

Article Info: *Revised* : November 9, 2011. *Published online* : November 30, 2011

1 Introduction

Today, several approaches, of the Lagrangian [23], ALE [19, 20] and SPH [20, 15, 14, 8] types, aim to understand the soft shocks on structures.

One of the main application of these studies is the effect of bird impacts, pieces of tire or hailstone on aeronautical structures. The first difficulty of these studies is that these impacts have a variation of the spatio-temporal loading. Moreover, the second difficulty, with continuous approaches, is the definition of the theirs behaviour law, that is intrinsically a multi-body object. This study proposes the used of Discrete Element Method (DEM) to simulate this kind of impactor. In this first step, the impactor is simplified into a bag filled with spherical discrete elements. The aim at this stage is to derive a mathematical model of spatio-temporal loading, which can then be used to provide input to a numerical model with a deformable target. It is shown how the spatio-temporal loading law can be complex with this kind of impactor.

Introduced by Cundall in 1979 [3], the Discrete Element Method has since been developed for its application to increasingly varied problems, such as those given in the following examples: the simulation of damage, failure and fragmentation in concrete structures [28, 4, 5], the analysis of geomechanical problems [27, 26], the simulation of manufacturing processes for textiles, and the determination of the micro-geometry of manufactured textiles [32, 33, 24], the study of contact problems [6, 7, 11], the analysis of composite material cutting processes [10] , or the study of impact problems [22, 18, 29]. An asset of this method is its ability to extract the macroscopic behaviour of a material or a structure, based on the interactions of microscopic particles, for which the geometric and interaction models are simple. In the case of impact problems, the Discrete Element Model has been successfully used for the simulation of the impacted structure [28, 29] and the impactor is generally considered as a rigid body. In the case of the considered impact, the impactor behaviour is complex and this study focuses on impactor behaviour using DEM approach.

Two types of particle geometry are generally used with the DEM: spherical [27, 29, 11] or polyhedral [4, 5], with the problem of contact between particles clearly being simpler to treat in the case of spherical particles. For this application, spherical discrete elements are thus used. Simple interaction rules are introduced, at the scale of the discrete element, to represent the more

complex behaviour of the impactor at the macroscopic scale. The proposed analysis is mainly phenomenological, in order to provide an understanding of how the geometrical and the mechanical parameters can influence the spatio-temporal loading history during a "soft" shock.

When using DEM, the generation of the simulated domain is generally not geometrical as a mesh in Finite Element Method. The domain is the result of an initial calculation. Thus, the geometrical domain generation is first presented. The interaction laws between discrete elements determine the macroscopic behavior. These laws are presented in a second time. Finally, the method for post-treating the calculation is given. It allows the study of loading history at the impactor/target interface. A qualitative analysis of the numerical results is given and the complexity of contact behavior is outlined.

2 Geometrical modeling of the impactor

The impactor is made of a set of discrete elements of spherical geometry (Figure 1), called grains or particles. Its initial general form is also a sphere, of radius R_0. Two particle subsets form the impactor: the first defines its envelope, and the second represents the particles inside the sphere, the boundary of which is formed by the envelope. The particles belonging to the envelope will be noted by pe, and the others by ps.

In order to ensure its cohesion, the envelope is made of pe particles connected to each other by bonds. Each particle has N bonds with its neighbours. A bond between two particles i and j, with centers at G_i and G_j respectively, is a spring attached to the centers of the two particles.

2.1 Generation of the pe particles

The pe particles are generated with a unique radius r_{pe}, and are then geometrically distributed in space so as to form the spherical envelope (Figure 2). Only one layer of pe particles in thickness is considered to obtain a membrane behaviour of the envelop. Using a spherical coordinate system (r, θ, ϕ), the pe particles are positioned without contact on an imaginary grid, which is a sphere of radius $R_{pe} = R_0 - r_{pe}$ centered at O.

The *pe* particles are generated along the successive longitudes ϕ (with $-\pi/2 \leq \phi \leq \pi/2$). For a given longitude ϕ the number of particles N_{pe} juxtaposed on the circle with center A and circumference $C_A = 2\pi R_{pe} sin\phi$ is approximated by $Integer\ Part\,(C_A/2r_{pe})$. The angle $\left(\widehat{G_i, A, G_j}\right)$ between two particles i and j, with respective centers G_i and G_j, separated by $\delta\theta$ is thus equal to $2\pi/N_{pe}$.

Similarly, the angle between two neighboring longitudes separated by $\delta\phi$ is equal to $2\pi/N_\phi$, where $N_\phi = Interger\ Part\,(2\pi R_{pe}/2r_{pe})$.

2.2 Generation of bonds between the *pe* particles

To ensure the cohesion between all particles, bonds are created between each *pe* particle and N close neighbours. Each bond acts as a traction/compression spring. Depending on the number of bonds chosen per particle, the rigidity of the envelop will be changed. In the following, different configuration are generated. These are referred to as an envelope with N bonds ($0 \leq N \leq 6$), with N an integer corresponding to the number of bonds per particle.

First of all, a 6-bond configuration is generated, and is used as a base. Then, for each particle i, a maximum of $6 - N$ bonds are removed by random selection, such that each particle has a minimum of N bonds.

2.3 Generation of the *ps* particles

The generation of the initial domain with spherical particles of different size is always a key difficulty when using DEM and must be carried out carefully. For this study, the proposed procedure allows to obtain :

1. an initial packing of the domain between 55% and 58%,
2. a negligible internal potential energy compared to the impact energy of the numerical experience.

The set comprising the *ps* particles contained by the sphere, defined by the envelope of radius $R_0 - 2r_{pe}$, is constructed as follows (Figure 3) :

- firstly, a spherical domain larger than that required is generated by juxtaposing particles; this domain is constructed by stacking circumferential

layers, each layer being constructed by the same method as that used to generate the particles of the envelope;

- the radius r_{ps} of each particle is allocated randomly, from a uniform distribution over the interval $[r_{mean} - \delta r, r_{mean} + \delta r]$ where r_{mean} represents the mean radius of the *ps* particles; variations in the diameter of these particles avoids organisation effects, i.e. the appearance of aligned structural portions, to be avoided;

- in an effort to obtain a domain having characteristics independent from the initial geometry, the spherical domain is then compacted by means of a DEM [11] computation : a virtual spherical wall, considered as a specific discrete element, contains the *ps* particles within the volume defined by its surface; a hydrostatic pressure p is imposed on the external surface S of this wall; the global geometry of the wall remains spherical as a function of time, even when the radius of the sphere varies according to the hydrostatic pressure p applied to the external surface, until stable equilibrium is achieved; the dynamic equilibrium of the wall, governed by equation 1, is thus computed globally:

$$\int_S \left(-p\overrightarrow{e}_r\right) dS + \sum_i \overrightarrow{f}_{i\to wall} = \int_S \left(\rho_S \overrightarrow{\gamma}_{wall}(\theta,\phi)\right) dS \qquad (1)$$

where $\overrightarrow{e}_r$ is the normal to the walls surface at a point M, $\overrightarrow{f}_{i\to wall}$ is the force imparted by the particle i to the wall, ρ_S is the surface density of the wall and $\overrightarrow{\gamma}_{wall}(\theta,\phi)$ is its acceleration at point M; in addition, to simplify mixing of the particles:

  - the pressure applied to the wall oscillates with a pulsation ω and an amplitude Δp : $p = p_0 + \Delta p \cdot sin(\omega t)$;
  - at each iteration, a small Brownian movement is added to the particle movements computed by the DEM algorithm:

$$x^t_{ps} = x^t_{DEM} + \Delta x; \quad y^t_{ps} = y^t_{DEM} + \Delta y; \quad z^t_{ps} = z^t_{DEM} + \Delta z \qquad (2)$$

    x^t_{ps}, y^t_{ps} and z^t_{ps} being the coordinates of the center of the *ps* particles at time t, x^t_{DEM}, y^t_{DEM} and z^t_{DEM} being the coordinates of the particles derived from the DEM calculation at time t and Δx, Δy

as well as Δz being small additional displacements drawn at random from a uniform distribution over the interval $]0, b_{max}]$ (where b_{max} is a constant).

Normally, domain mixing occurs only with the help of non-spherical walls, whether virtual or not, which vibrate or are in movement (in the case of non virtual walls [11]); the addition of a Brownian type of movement to the DEM calculation is original and enables quite rapid convergence to be achieved for the compaction computation;

- the final set of *ps* particles is defined starting from this compact spherical domain: only those particles satisfying the relationship $(R_{pe} - r_{pe} - d - r_{ps}) \geq 0$ are retained, where d is the distance separating the center of the particle from the center of the impactor;

- at the end of the compacting stage, the configuration of the *ps* particles is frozen, although a number of these are interpenetrated; these interpenetrations lead to interaction forces (presented in § 3) thereby producing internal potential energy which must be minimized before the impact simulation is run; in order to "relax the stresses" and thus release part of this potential energy, a new DEM calculation is carried out; the radius of the virtual wall is constant during the calculation; repulsive and dissipative forces defined in § 3.1 are expressed by means of exponential laws in this relaxation calculation, in order to minimize the particle interpenetrations and maximize energy dissipation; although the time step in the solving algorithm is chosen to be very small, in order to ensure stability of the computation, convergence is achieved rapidly.

3 Mechanical modeling of the impactor: Interaction forces

Particle interaction laws are introduced, thus allowing the global behavior of the impactor to be represented. These are related to interactions between the *ps* particles, between the *pe* particles, between the *pe* and *ps* particles, and between the *pe* particles and the target.

These interactions result in forces of three different types: compressive, dissipative, and tensile forces. The *pe* particles can experience these three types of interactive force, with the tensile forces being provided by means of their bonds, whereas the *ps* particles can only experience compressive and dissipative forces through contact. Many models describing these interactions are presented in [17]. They can be classified into four main categories: models based on continuous potential energy [1], linear visco-elastic models [16, 21], nonlinear visco-elastic models [2], and finally so-called hysteresis models [30]. Nevertheless, in the present study, simple models of the linear visco-elastic type, proposed by [11], have been used to describe the forces.

3.1 Compressive and dissipative forces

Compressive and dissipative forces appear when a particle i and an object j, with j being either a particle or the *target*, are in contact. These forces, noted respectively by $\overrightarrow{F}_{i\to j}^{comp}$ and $\overrightarrow{F}_{i\to j}^{dis}$, and indicating the action of the particle i on the object j, are defined as:

$$\overrightarrow{F}_{i\to j}^{comp} = F_{i\to j}^{comp}\overrightarrow{n} \quad \text{et} \quad \overrightarrow{F}_{i\to j}^{dis} = F_{i\to j}^{dis}\overrightarrow{n} \tag{3}$$

where $\overrightarrow{n} = \dfrac{\overrightarrow{G_iG_j}}{\|\overrightarrow{G_iG_j}\|}$ when interaction forces between particles are described, and $\overrightarrow{n} = \overrightarrow{z}$, the normal to the plane of impact, in the case of interaction forces between *pe* particles and the target.

Simple models are used to express $F_{i\to j}^{comp}$ and $F_{i\to j}^{dis}$:

- $F_{i\to j}^{comp}$ is expressed using the stiffness K of a spring under compression and the interpenetration δ_{nc} of two particles i and j or the penetration of a particle i on the target, with j then referring to the target (Figures 4(a) and 4(b)):

  $$F_{i\to j}^{comp} = K \times \delta_{nc} \tag{4}$$

  In the case of an interaction between two particles i and j, K has the equivalent stiffness of two springs in series, using the stiffnesses K_i and K_j, associated with the two particles:

  $$K = \frac{K_i \times K_j}{K_i + K_j} \tag{5}$$

In the case of an interaction between two particles i and a target of infinite rigidity; K is equivalent to K_i^p, the contact stiffness between the particle i and the rigid, flat target (Figure 4(b)):

$$K = K_i^p \tag{6}$$

The stiffness of a particle i experienced during a sphere / sphere or a sphere / plane contact is given by the empirical law $E \cdot r_i$ [11], where E is Youngs modulus for the material of particle i; K_i and K_i^p are then equal to $E \cdot r_i$;

- The dissipation of energy is represented by viscous damping. $F_{i\to j}^{dis}$ can be expressed as:

$$F_{i\to j}^{dis} = 2\alpha\sqrt{KM_{ij}} \times \dot{\delta}_{nc} \tag{7}$$

where α is the dimensionless damping coefficient (< 1), $\dot{\delta}_{nc}$ is the relative velocity of the two particles i and j, of respective mass m_i and m_j, and M_{ij} is the equivalent mass; in the case of an interaction between two particles, the equivalent mass is equal to:

$$M_{ij} = \frac{m_i \times m_j}{m_i + m_j} \tag{8}$$

In the case of an interaction between a particle i and a target of infinite rigidity, j, this is defined by:

$$M_{ij} = m_i \tag{9}$$

the coefficient α is directly related to the energy restoration coefficient used in kinetic models [25, 13].

3.2 Tensile forces

For the set of *pe* particles belonging to the envelope, when a bond joining a particle i to a particle j is under tension, a tensile force $\overrightarrow{F}_{i\to j}^{tens}$ is created (Figure 4(c)), as defined by:

$$\overrightarrow{F}_{i\to j}^{tens} = K \times \delta_{nt} \cdot \frac{\overrightarrow{G_iG_j}}{\|\overrightarrow{G_iG_j}\|} \tag{10}$$

where δ_{nt} represents the bond stretching and K is an equivalent tensile force stiffness between a *pe* particle i and a *pe* particle j. Consequently, the stiffness of a particle i experiencing a tensile force is equal to $E \cdot r_i$ and the equivalent stiffness is given by equation 5.

4 Determination of the loading at the impactor-target interface

4.1 Computational algorithm

The algorithm used is of the explicit type. It runs according to the following steps:

- at a time t the coordinates (x_i^t, y_i^t, z_i^t) of the center G_i^t of each particle i are known; for each contact identified between two particles, or between a particle and the target, the interpenetration δ_{nc} is computed; similarly, if the bond between two particles is under tension the parameter δ_{nt} is computed;

- using equations (4), (7) and (10) it is then possible to compute the forces $\overrightarrow{F}_{i\to j}^{comp}$ and $\overrightarrow{F}_{i\to j}^{dis}$ applied at the center of each *pe* and *ps* particle, as well as the forces $\overrightarrow{F}_{i\to j}^{tens}$ applied at the center of each *pe* particle; at an instant t the resultant of these forces for a particle i will be written as $\overrightarrow{F}_i^t$;

- as interaction forces are now known, the accelerations $(\ddot{x}_i^t, \ddot{y}_i^t, \ddot{z}_i^t)$ at the particles center are determined according to Newtons second law:

$$\ddot{x}_i^t = \frac{F_{ix}^t}{m_i}, \quad \ddot{y}_i^t = \frac{F_{iy}^t}{m_i}, \quad \ddot{z}_i^t = \frac{F_{iz}^t}{m_i} \tag{11}$$

  where F_{ix}, F_{iy} and F_{iz} denote the components of $\overrightarrow{F}_i^t$ along $\overrightarrow{x}$, $\overrightarrow{y}$, $\overrightarrow{z}$, respectively;

- Finally, Verlets [31] temporal integration method is used to integrate the velocity of the particles and to derive their new coordinates $\left(x_i^{t+dt}, y_i^{t+dt}, z_i^{t+dt}\right)$ at time $t + dt$, with dt indicating a time increment;

- The solving algorithm stops when the impactor rebounds, i.e. either as soon as the reaction of the impactor on the target is zero, for a duration of ΔT_{stop}, or when the maximum number of iterations has been reached.

4.2 Determining the impactor/target reaction

The aim is to derive from the modulus of the "macroscopic"' force F_{macro} applied by the impactor to the target, starting from the mesoscopic scale interactions between the *pe* particles of the envelope and the target. This macroscopic force, referred to as the impactor/target reaction, is derived from the spatial summation, and temporal average of the stresses $\overrightarrow{F}^{comp}_{i\rightarrow target} + \overrightarrow{F}^{diss}_{i\rightarrow target}$ exerted by the particles on the target:

$$F_{macro} = \frac{1}{\Delta T} \sum_{t_k}^{t_k+\Delta T} \sum_{i=pe} || \overrightarrow{F}^{comp}_{i\rightarrow target} + \overrightarrow{F}^{diss}_{i\rightarrow target} || \tag{12}$$

Time averaging allows the effects of characteristic vibrations at the scale of a grain to be avoided: the data is averaged over a period of $\Delta T = 100 \times T_c$, where T_c is a reference time characterizing the mean oscillatory period due to the mass-spring system governing the contact between two grains [11]. ΔT must be sufficiently long with respect to T_c, but also sufficiently short to provide an adequate representation of F_{macro}: the distance traveled by a *ps* particle during ΔT with an initial velocity $\bar{v}_0$, must be of the order of the size of the particle.

4.3 Determination of the contact zone at the impactor/ target interface

The problem involves determining the spatial distribution of contacts between impactor particles and the target, in order to evaluate, at the macroscopic scale, the extent of the contact surface between the impactor and the target.

A time average is determined in order to avoid characteristic vibration effects at the scale of a grain: a particle i of the envelope may have several points of contact with the target over a period ΔT; the position of these different contact points are thus averaged over the period ΔT.

In order to represent the contact surface between the impactor and the target, the spatial distribution of the particle/target contacts is encompassed by two circles of radii R^c_{int} and R^c_{ext}, defining a ring (Figure 5(a)):

- The interior radius of the ring, R^c_{int}, corresponds to the radius of a circle passing through the particle-target point of contact closest to the center O' which is the projection of O, the center of the sphere at the initial time (Figure 5(b)).
- Similarly, the outer radius of the ring, R^c_{ext}, corresponds to the radius of a circle passing through the particle-target point of contact most distant from the center O';

R^c_{int} and R^c_{ext} are evaluated starting from the mean positions of the particle/target contacts. This representation of the contact surface is simple and efficient for comparing the evolution of the contact surface during the parametric analysis presented in the following. Detailed analysis of the contact point distribution will enable additional information to be extracted locally.

4.4 Determination of the spatial distribution of stress

The aim is to determine, at a given time point, the spatial variation of the loads applied to the target by the impactor. However, in terms of memory, it is not possible to save each contact point between the *pe* particles and the target, as well as the corresponding forces. The proposed solution consists in meshing the target, and projecting the particle / target interaction forces onto the nodes of this mesh. Thus, only the loads generalized at the nodes are recorded. The second advantage of this method is that it introduces spatial smoothing onto the load variation curves, thereby attenuating the particle-like appearance of the envelope.

In this initial feasibility step, the target, assumed to be rigid, is regularly discretized with linearly interpolated 4-node elements. When contact occurs between a particle i and the target, the force $\overrightarrow{F}^t_{i\rightarrow target}$ exerted by particle i on mesh m, at time t, is then projected onto the interpolation function (linear here) basis, of the element to which it is applied. Over a period ΔT, when several contacts occur between particles and the mesh element m, the forces projected onto the nodes are summed, following which a temporal average is

computed over ΔT. The reduced force F_{nm} computed at node n of mesh m is thus of the form:

$$\overrightarrow{F}_{nm} = \frac{1}{\Delta T} \sum_{t_k}^{t_k+\Delta T} \sum_{i} \overrightarrow{F}^{t}_{i \to m} \cdot N_{nm} \tag{13}$$

N_{nm} is the linear interpolation function associated with node n of mesh m. The spatial distribution of the loading is thus given by the knowledge of the values $\overrightarrow{F}^{t}_{nm}$ at the nodes n of the contact area.

5 Qualitative analysis of loading

5.1 Simulations

To simplify the following parametric analyses, the system parameters are dimensioned according to three characteristic quantities, as in [12]: the mean radius r_{mean} of particles ps, the reference mass for the particles $m_{ref} = \frac{4}{3}\pi r^3_{mean}\rho_{ref}$ and the characteristic oscillation time due to the mass - spring system controlling the contact between two particles, with $T_c = 2\pi\sqrt{\frac{m_{ref}}{K_{mean}}}$, K_{mean} being the particles' mean stiffness. In the following, r_{mean}, ρ_{ref} and K_{mean} are assumed to be equal to 1.

Impactors with a variable initial radius R_0 and mass M_T are projected with an initial dimensionless velocity $\overrightarrow{v}_0 = -|\bar{v}_0|\,\overrightarrow{z}$ onto a perfectly rigid target located in the plane $z = 0$ (Figure 5(b)). The initial distance h_0 between the center of the impactor and the target is $R_0 + 2000 \times r_{mean}$. The first instant of contact between the impactor and the target thus occurs at $t = 2000$.

In addition, the total mass M_T of the impactor is equal to the sum of the masses m_i of the particles $i = peUps$, in other words:

$$M_T = \sum_i m_i = \sum_i \frac{4}{3}\pi r_i^3 \cdot \rho_i \tag{14}$$

with ρ_i designating either ρ_{pe} or ρ_{ps}, respectively, that is the volume density of the pe or ps particles.

Finally, the time step dt used in the numerical simulation must be significantly smaller than T_c, in order for contacts between particles to be correctly taken into account. A convergence study of the impactor/target reaction F_{macro}, computed for a shock with an impactor of radius $R = 21 \times r_{mean}$, shows that a time step dt of $\frac{1}{10}T_c$ is sufficient for these simulations.

5.2 Parametric analysis

With a view to qualitatively analyzing the change in loading during a shock, a parametric analysis was carried out with respect to two sets of parameters:

- A set of so-called intrinsic (or mesoscopic) parameters:
    1. the number of bonds N per envelope particle; the case for which there is no bond between envelope particles ($N = 0$) has also been simulated;
    2. the characteristic dimension of the envelope particles r_{pe}, with a constant mean ps particle radius: $r_{mean} = 1$; the mean radius of the balls remains constant for these simulations: $r_b = 1$;
    3. the mean respective stiffnesses $K_{pe} = E_{pe} \cdot r_{pe}$ and $K_{ps} = E_{ps} \cdot r_{ps}$ of the pe and ps particles; E_{pe} and E_{ps} are the Young's moduli of the materials used for the particles pe and ps, respectively;
    4. the volume densities ρ_{pe} and ρ_{ps} of particles pe and ps, respectively;
- A set of "macroscopic" parameters:
    1. the initial velocity $\bar{v}_0$ of the impactor;
    2. the total mass of the impactor M_T,
    3. the initial radius of the impactor R_0.

The simulations carried out for the sensitivity analysis of the intrinsic parameters made use of an initial impactor radius of $R_0 = 21 \times r_{mean}$, and a mass $M_T = 10000$ (except for the study of the volume densities ρ_{pe} and ρ_{ps}) and finally an incident velocity $\bar{v}_0 = 0.001$. The numerical simulations are summarized in Table 1.

Table 1: Starting parameter values for the sensitivity analysis of the mesoscopic parameters

	N	r_{ps}	r_{pe}	E_{ps}	E_{pe}	ρ_{ps}	ρ_{pe}
(1)	0, 3, 4, 5, 6	1	0.25	1	1	8.45	8.45
(2)	4	1	1, 0.5, 0.25	1	1	8.45	8.45
(3)	4	1	0.25	1, 0.005	0.005, 1	8.45	8.45
(4.a)	4	1	0.25	1	1	8.45	8.45, 16.91, 121.06
(4.b)	4	1	0.25	1, 0.005	0.005, 1	8.45, 16.91	8.45

The simulations carried out for the sensitivity analysis of the macroscopic parameters made use of number of bonds per particle $N = 4$, a pe radius of $r_{pe} = 0.25$, a ps mean radius of $r_{ps} = 1$, a Young's modulus for the particles $E_{pe} = E_{ps} = 1$ and a mass per unit volume for the particles $\rho = \rho_{pe} = \rho_{ps}$.

The details of the numerical simulations are summarized in Table 2 :

1. For simulations $t1$, $t2$, $t3$, only the initial velocity is modified ($\bar{v}_0 = 5.10^{-4}$, 10^{-3} and 5.10^{-3}), with the other parameters remaining constant ($M_T = 10^5$ and $R_0 = 21 \times r_{mean}$);

2. For simulations $t2$, $t4$, $t5$, the total mass of the impactor ($M_T = 10^5$, 5.10^5 and 10^6) varies with the mass per unit volume of the particles ($\rho =$ 8.45, 42.27 and 84.54), with the other parameters remaining constant ($\bar{v}_0 = 10^{-3}$ and $R_0 = 21 \times r_{mean}$);

3. For simulations $t6$, $t2$, $t7$, the initial radius of the impactor varies ($R_0 =$ 11, 21 and $31 \times r_{mean}$), with the other parameters remaining constant. ($\bar{v}_0 = 10^{-3}$ et $M_T = 10^5$);

Table 2: Starting parameter values for the numerical simulations

n° test	t1	t2	t3	t4	t5	t6	t7
$\bar{v}_0$	5.10^{-4}	10^{-3}	5.10^{-3}	10^{-3}	10^{-3}	10^{-3}	10^{-3}
R_0 ($\times r_{mean}$)	21	21	21	21	21	11	31
ρ	8.45	8.45	8.45	42.27	84.54	8.45	8.45
M_T	10^5	10^5	10^5	5.10^5	10^6	13076.3	332281
Total number of particle	26944	26944	26944	26944	26944	6643	64932

5.3 Results

Firstly, some general comments are made concerning the appearance of the derived curves, before discussing the influence of the "mesoscopic" and "macroscopic" parameters.

5.3.1 General comments

Overall, the curves F_{macro} obtained as a function of time (Figure 6(a), 8, 9, 10, 11, 12(a), 13(a), 14 and 15(a)) have the same general appearance, which remains consistent with that generally found in the case of an impact [9]. They also reveal oscillations, which are representative of vibratory signals associated with propagation and wave interference in the medium formed by the *ps* and *pe* particles. These oscillations, in addition to their numerical origin, can also be explained by the simultaneous progression of the impactor/target contact surface and of the loads imposed by the particles on the target. This oscillatory phenomenon is all the more noteworthy, because the contact times are long.

In addition, the curves showing the time variation of F_{macro} have two distinct maxima, occurring at times T_1 and T_2, with the second of these having a greater amplitude than the first.

The presence of these two maxima can be explained by comparing the variation in geometry of the impactor with that of the contact surface (Figures 6(a) and 6(b)). Indeed, it is interesting to note that the maximum radius of the impactor, $R_{max}^{impactor}$, hardly varies until the instant T_1, and then increases almost linearly until reaching its maximum value at T_2. As a result, the deformation of the impactor is contained in a region close to the impactor/target contact

point until time T_1. Thereafter, between T_1 and T_2, the impactor will increasingly flatten out onto the target until it reaches a maximum compression state at time T_2.

In parallel with the impactor/target reaction, there is a considerable variation in the contact surface between the impactor and the target (Figures 6(b), 12(b), 13(b) and 15(b)), simply represented here by the variations of the interior and exterior radii R^c_{int} and R^c_{ext} (section 4.3). Consequently, with the exception of the first instants of impactor/target contact, R^c_{int} is non-zero, but remains small with globally small variations; its evolution is nevertheless perturbed as a result of contact fluctuations between the particles and the target at the center of the contact surface. Additionally, R^c_{ext} has only one maximum, which occurs at the time instant T_2; at this instant, R^c_{ext} is of the order of magnitude of the initial radius of the impactor R_0, thus revealing the soft nature of the impact, as shown by the large contact surface area.

On the other hand, the curve F_{macro} tends to 0 after the first peak, which does not necessarily indicate a rebound of the impactor, since in most of the cases presented here the latter is still in contact at the end of the computation. The notion of a contact time is then introduced, based on the variations of the F_{macro} curve after the second instant T_2. This is shown by the time instant T_3, where F_{macro} is equal to 2% of the maximum force, which was previously computed at time T_2.

Finally the spatial distribution of the contact loading at the impactor/target interface can be seen at instants T_1 and T_2 in Figures 7(a) and 7(b). This distribution is not homogeneous, and does not resemble the general behavior of the Hertz contact of a sphere on a plane. This result can in particular be explained by the fact that the impactor is a bag of roller balls, and that the particle characteristics of its elements can be found in the discrete shape of the distribution.

5.3.2 Influence of the number N of bonds per envelope particle

There is no visible second peak on the curve of F_{macro} (Figure 8) when $N = 0$. The second peak associated with the compression of the impactor on the target can thus not occur without taking into account the role of the bonds which ensure cohesion of the envelope.

In addition, the beginning of each curve ($N = 0, ..., 5$) is almost identical

up until the appearance of the second peak. On the other hand, the role of the bonds, in the mechanism leading to the occurrence of the first peak, is thus minimal.

Finally, the greater the value of N the earlier the temporal occurrence of the second peak. For $N = 6$, the first and second peaks nearly coincide. This corresponds to an increase in the stiffness of the envelope and a decrease in the "soft" effect of the impact.

5.3.3 Influence of the radius r_{pe} of the pe particles

The influence of this parameter can be seen in Figure 9. By decreasing the radius of the pe particles, the maximum of the F_{macro} curve at instant T_2 increases, whereas that occurring at instant T_1 does not change significantly. However, by decreasing r_{pe} there is an increase in the number of pe particles forming the envelope, as well as in the total number of bonds between pe particles. As discussed earlier in this section, the total number of bonds has an influence on the variations in the second maximum of the F_{macro} curve.

In addition, the computed curves are less noisy when the radius r_{pe} decreases, which is probably the consequence of an increase in the number of pe particle/target contacts at each iteration, which results in smoothing of the curves. The same phenomenon is observed for the variation curves of the contact surface area between the impactor and the target (not shown here).

5.3.4 Influence of the mean respective stiffnesses K_{pe} and K_{ps} of the pe and ps particles

According to the curves shown in Figure 10, by reducing the stiffness K_{pe} of the pe particles, for a constant stiffness value K_{ps} the resulting curve shows fewer oscillations and a smoother appearance; the amplitude of the curve and the times at which the maxima occur remain approximately unchanged. As the pe particles are those which enter directly into contact with the target, their characteristic oscillatory period $t_{pe} = 2\pi\sqrt{m_{pe}/K_{pe}}$ is a parameter which must have a strong influence on the oscillations visible on the curves; indeed, by decreasing K_{pe}, t_{pe} increases, which may be the explanation for the smooth appearance of the curve.

Moreover, by increasing K_{ps}, this time maintaining K_{pe} constant, the am-

plitude decreases slightly, and a shift in time can be observed (the time needed to produce the maxima is greater).

5.3.5 Influence of the respective densities ρ_{pe} and ρ_{ps} of the pe and ps particles

As observed in Figure 11, the response of the impactor is more sensitive to the density of the ps particles than to that of the pe particles: when ρ_{pe} is multiplied by two, there is no noteworthy change in the curve. However when ρ_{ps} is multiplied by two, the amplitude of the curve is virtually doubled. Nevertheless, the increase ΔM_T in total impactor mass is relatively small when ρ_{pe} is multiplied by two ($\Delta M_T = 6528$), when it is compared with that arising when ρ_{ps} is multiplied by two ($\Delta M_T = 93472$). Indeed, the total volume occupied by the pe particles is small in comparison with that occupied by the ps particles. For a constant value of ρ_{ps} the value of ρ_{pe} must therefore be multiplied by 15 in order to achieve an equivalent increase in mass ΔM_T. The amplitude of the second peak is then equivalent to that observed when ρ_{ps} is multiplied by two, but the amplitude of the first peak remains slightly lower, the curve exhibits strong oscillations, and the second peak occurs later in time. The last two changes are due to the high value of ρ_{pe} used in the calculation.

5.3.6 Influence of the initial velocity $\bar{v}_0$ of the impactor

The curves shown in Figure 12(a) reveal tendencies already known in the case of a shock involving rigid impactors on a deformable target [9]. Indeed, the greater the incident velocity, the shorter the contact time, and the greater the resulting force of the impact. Similarly, the time interval between the instants T_1 and T_2 decreases when the velocity increases.

In addition, in Figure 12(b), the maximum contact surface area at time T_2 does not appear to be affected by the velocity $\bar{v}_0$, over the studied range.

5.3.7 Influence of the mass M_T of the impactor

The curves shown in Figure 13 and 14 have a generally identical appearance, with identical instants in time for the occurrence of the two peaks, plotted with respect to the mass M_T of the impactor. This shows that, apart from small

differences due to oscillations, the contact force appears to be almost proportional to the mass of the impactor. Furthermore, the parameter M_T has only a minor influence on changes in the contact surface area. This is a surprising result, in view of the fact that an increase in the impactor's mass leads to an increase in its inertia. This outcome will need to be further investigated in future studies, before it can be validated.

5.3.8 Influence of the initial radius R_0 of the impactor

The influence of this parameter is visible in Figure 15. The greater the radius of the impactor, the greater the increase in contact time (T_3) and occurrence times (mainly T_2) and the more the contact force increases. At the instant at which the second maximum T_2 occurs, the external radius R^c_{ext} is of the order of magnitude of the initial radius R_0 of the impactor.

6 Conclusions and future outlook

In this study, an application of the spherical Discrete Element Method is proposed for the qualitative study of a "soft" shock. The modelized deformable impactor is a bag filled with spherical discrete elements. It impacted a rigid target. The main objective of the model is to determine the spatio-temporal loading at the impactor/target interface. Simple interaction laws are introduced at the scale of the particles. These interaction laws have enabled the macroscopic behavior of this impactor to be represented, and the impactor/target interface loading to be taken into account. The general appearance of the variation curves of this loading remains consistent with that previously reported in the literature [9], even if complementary investigations are needde when M_T varies, and thus confirms the relevance of the model. The qualitative analysis of these curves, produced by varying "mesoscopic" parameters (the number of bonds between *pe* particles, the size of the *pe*, particles, the respective stiffnesses of the *pe* and *ps* particles, as well as their densities), and their macroscopic parameters (initial velocity of the impactor, its mass and initial radius), reveals the existence of two specific instants in time, T_1 and T_2, associated with two distinct force levels. These peaks can be

explained by changes in the state of deformation of the impactor at the time of the shock: initially located in the zone close to the contact (instant T_1), the measured deformation then spreads over the impactor as it becomes progressively compressed onto the target, until such time (instant T_2) as it reaches maximum compression. In view of these highly interesting initial results, in qualitative terms, their experimental validation has now become a priority. As a follow-up of the present study, it is foreseen to carry out tests, in order to identify the model's mesoscopic parameters, for quantitative analysis of the spatio-temporal distribution.

References

[1] K.M. Aoki and T. Akiyama, Simulation studies of pressure and density wave propagations in vertically vibrated beds of granules, *Physical Review*, **E 52**, (1995), 3288-3291.

[2] N.V. Brilliantov, F. Spahn, J. Hertzsch and T. Poeschel, Model for collisions in granular gases, *Physical Review*, **E 53**, (2004), 5382-5392.

[3] P.A. Cundall and O.D.L. Strack, A discrete numerical model for granular assemblies, *Geotechnique*, **29**, (1979), 47-65.

[4] G. Cusatis, Z. Bazant and L. Cedolin, Confinement-shear lattice CSL model for fracture propagation in concrete, *Computer Methods in Applied Mechanics and Engineering*, **195**, (2006), 7154-7171.

[5] A. Delaplace and R. Desmorat, Discrete 3D model as complimentary numerical testing for anisotropic damage, *International Journal of Fracture*, **148**, (2008), 115-128.

[6] N. Fillot, I. Iordanoff and Y. Berthier, Kinetics of particle detachment :contribution of granular model, *Tribology and Interface Engineering Series*, **43**, (2003), 63-73.

[7] N. Fillot, I. Iordanoff and Y. Berthier, A granular dynamic model for the degradation of material, *ASME J. Tribol.*, **126**, (2004), 606-615.

[8] S. Georgiadis, A. Gunnion,R. Thomson and B. Cartwright, Bird-strike simulation for certification of the Boeing 787 composite moveable trailing edge, *Composite Structures*, **86**, (2008), 258-268.

[9] L. Guillaumat, Aide au prédimensionnement de structures composites impactées, *Mec. Ind.*, (2000), 235-240.

[10] D. Illiescu, *Approche expérimentale et numérique de l'usinage à sec des composites carbone/époxy*, PhD Thesis, LAMEFIP EA 2727 -ENSAM Bordeaux, Décembre-2008.

[11] I. Iordanoff, A. Battentier, J. Néauport and J.L. Charles, A discrete element model to investigate sub-surface damage due to surface polishing, *Tribology International*, **41**, (2008), 957-964.

[12] I. Iordanoff, N. Fillot and Y. Berthier, Numerical study of a thin layer of cohesive particles under plane shearing, *Powder Technology*, **159**, (2005), 45-54.

[13] I. Iordanoff and M.M. Khonsari, Granular lubrication : towards an understanding of the transition between kinetic and quasi-fluid regime, *ASME J. Tribol.*, **126**, (2004), 137-145.

[14] A.F. Johnson and M. Holzapfel, Modelling soft body impact on composite structures, *Composite Structures*, **61**, (2003), 103-113.

[15] G.R. Johnson, A.R. Stryck and S.R. Beissel, SPH for high velocity impact computations, *Computer Methods in Applied Mechanics and Engineering*, **139**, (1996), 347-373.

[16] H. Kruggel-Emden, E. Simsek, S. Wirtz and V. Scherer, Modeling of granular flow and combined heat transfer in hoppers by the Discrete Element Method (DEM), *Journal of Pressure Vessel Technology*, **128**, (2006), 439-444.

[17] H. Kruggel-Emden, E. Simsek, S. Rickelt, S. Wirtz and V. Scherer, Review and extension of normal force models for the Discrete Element Method, *Powder Technology*, **171**, (2007), 157-173.

[18] Ferenc Kun and Hans Herrmann, Transition from damage to fragmentation in collision of solids, *Physical Review E*, **59**, (1999), 2623-2632.

[19] B. Langrand, A.S. Bayart, Y. Chauveau and E. Deletombe, Penetration prediction of missiles with different nose shapes by the discrete element numerical approach, *Int. J. Crashworth*, **7**, (2002), 415-428.

[20] M.A. Lavoie, A. Gakwaya, M. Nejad Ensan and D.G. Zimcik, Validation of available approaches for numerical bird strike modeling tools, *International Review of Mechanical Engineering*, (2007), 380-389.

[21] S. Limtrakul, A. Boonsrirat and T. Vatanatham, DEM modeling and simulation of a catalytic gassolid fluidized bed reactor: a spouted bed as a case study, *Chemical Engineering Science*, **59**, (2004), 5225-5231.

[22] S.A. Magnier and F.V. Donzé, Numerical simulations of impacts using a discrete element method, *Mechanics of Cohesive-frictional Materials*, **3**, (1998), 257-276.

[23] S. Meguid, R. Mao and T. Ng, FE analysis of geometry effects of an artificial bird striking an aeroengine fan blade, *International Journal of Impact Engineering*, **35**, (2008), 487-498.

[24] Y. Miao, E. Zhou, Y. Wang and B. Cheeseman, Mechanics of textile composites: Micro-geometry, *Composites Science and Technology*, **68**, (2008), 1671-1678.

[25] B.K. Mishra and C.V.R. Murty, On the determination of contact parameters for the realistic simulation of tumbling mills, *Powder Powder*, **115**, (2001), 290-297.

[26] E. Onate and J. Rojek, Combination of discrete element and finite element methods for dynamic analysis of geomechanics problems, *Computer Methods in Applied Mechanics and Engineering*, **193**, (2004), 3087-3128.

[27] D. Potyondy and P. Cundall, A bonded-particle model for rock, *International Journal of Rock Mechanics and Mining Sciences*, **41**, (2004), 1329-1364.

[28] E. Schlangen and E.J. Garboczi, Fracture simulations of concrete using lattice models: Computational aspects, *Engineering Fracture Mechanics*, **57**, (1997), 319-332.

[29] W. Shiu, F. Donze and L. Daudeville, Penetration prediction of missiles with different nose shapes by the discrete element numerical approach, *Computers & Structures*, **86**, (2008), 2079-2086.

[30] C. Thornton and Z.M. Ning, A theoretical model for the stick/bounce behaviour of adhesive, elastic-plastic spheres, *Powder Technology*, **99**, (1998), 154-162.

[31] L. Verlet, Computer Experiments on Classical Fluids. I. Thermodynamical Properties of Lennard-Jones Molecules, *Physical Review*, **159**, (1967), 98-103.

[32] Y. Wang, Digital-element simulation of textile processes, *Composites Science and Technology*, **61**, (2001), 311-319.

[33] G. Zhou, Multi-chain digital element analysis in textile mechanics, *Composites Science and Technology*, **64**, (2004), 239-244.

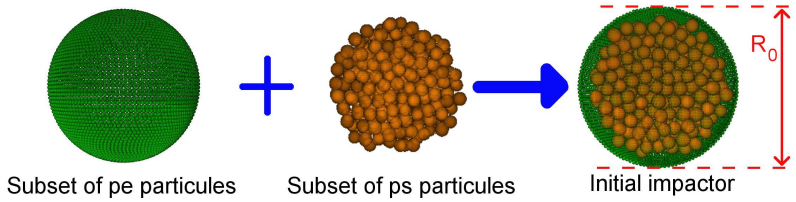

Figure 1: Two particle subsets form the impactor (diametrical scan)

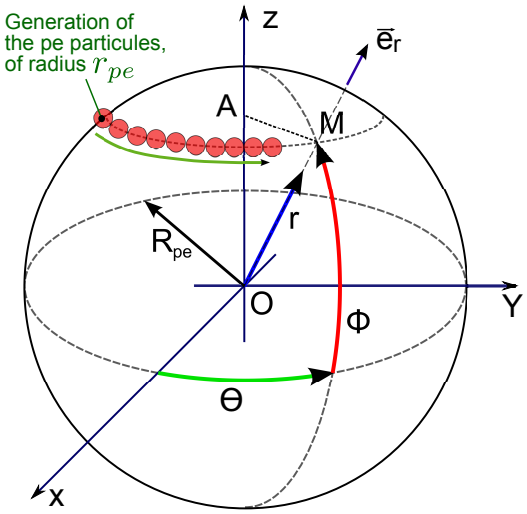

Figure 2: Generation of the *pe* particles subset

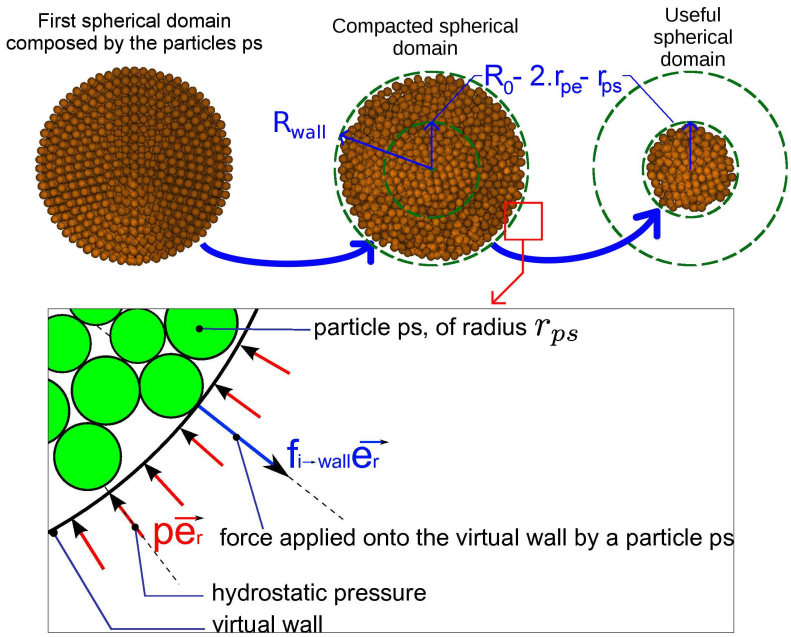

Figure 3: Generation of the *ps* particles subset and step to compact the spherical domain containing the *ps* particles (diametrical scan)

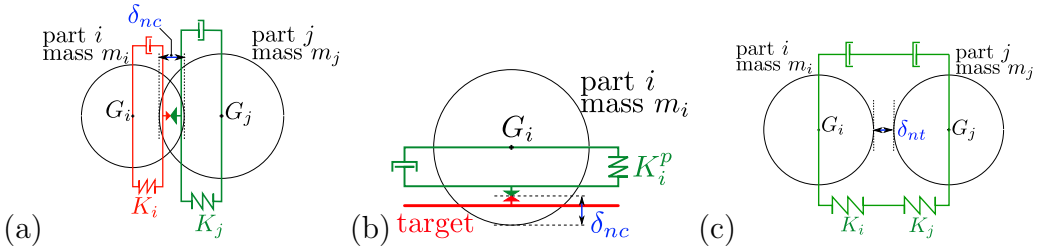

Figure 4: a) Contact between two particles b) contact between a *pe* particle and the target c) bond in tensile loading between two *pe* particles

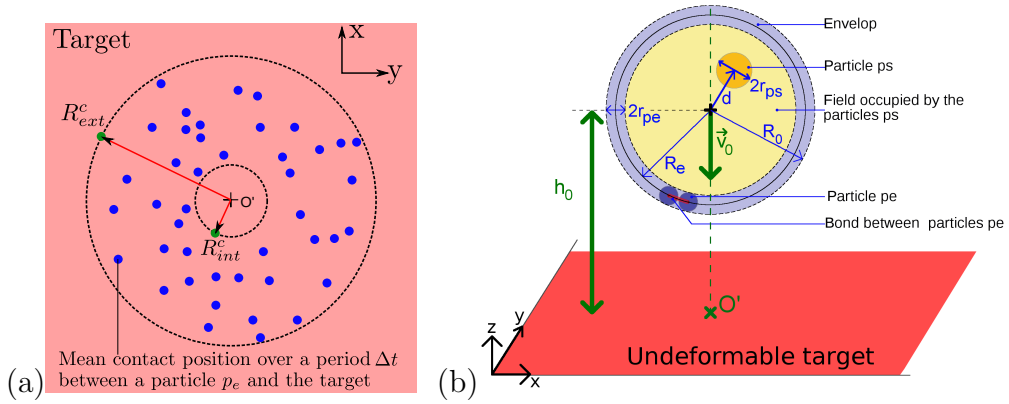

Figure 5: a) Mean contact area between the envelop and the target over a period Δt b) impactor and target

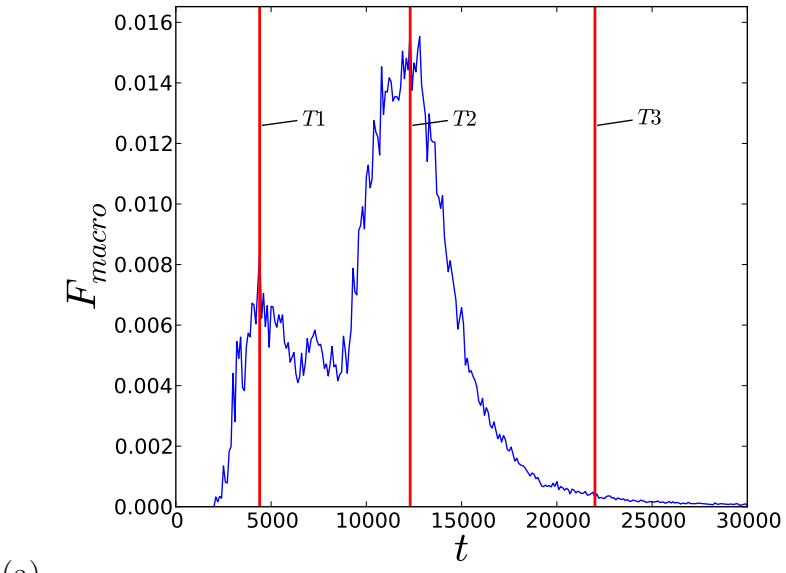

(a)

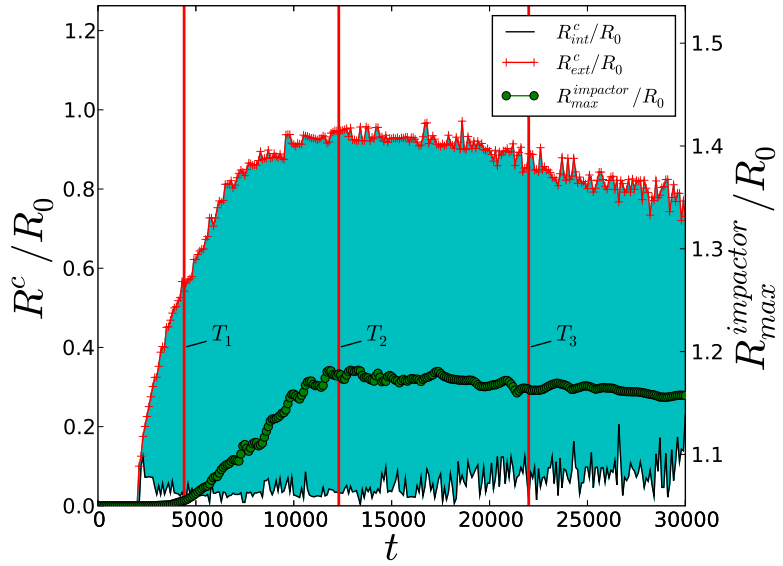

(b)

Figure 6: a) Time history of the load F_{macro}, imposed onto the target by the impactor; b) time history of the contact radius R^c_{int} and R^c_{ext}, between the target and the impactor, as well as the time history of the maximum radius of the impactor $R^{impactor}_{max}$.

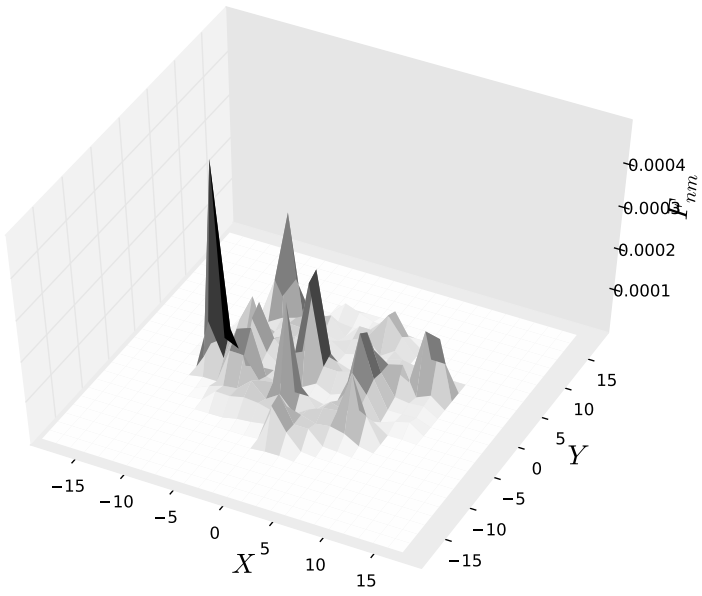

(a)

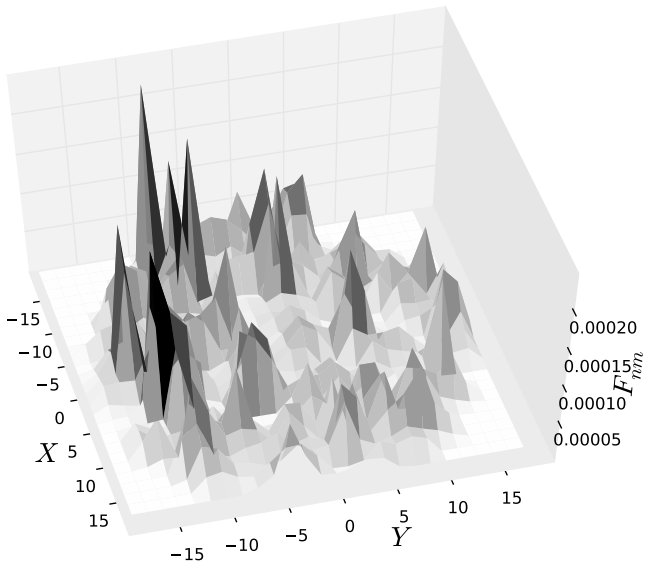

(b)

Figure 7: Discrete representation of the loading applied by the impactor (via the envelop) onto the target a) $T = T_1$ et b) T_2.

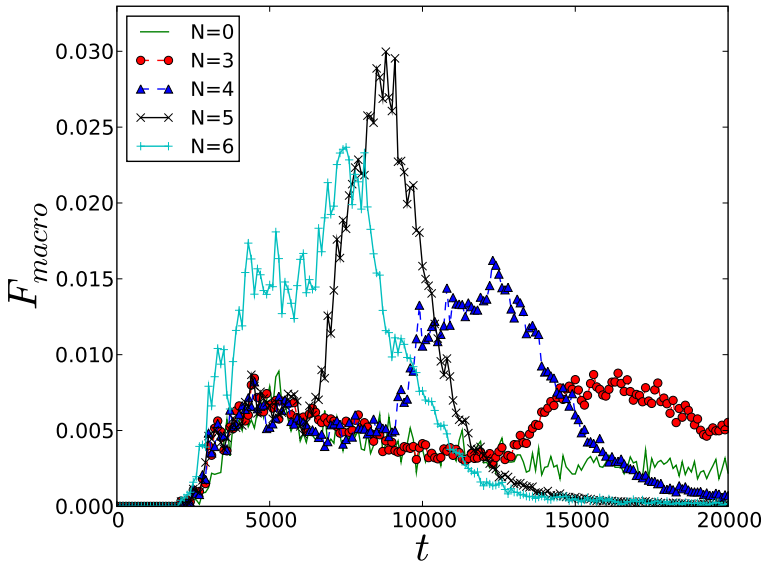

Figure 8: F_{macro} time history when N varies.

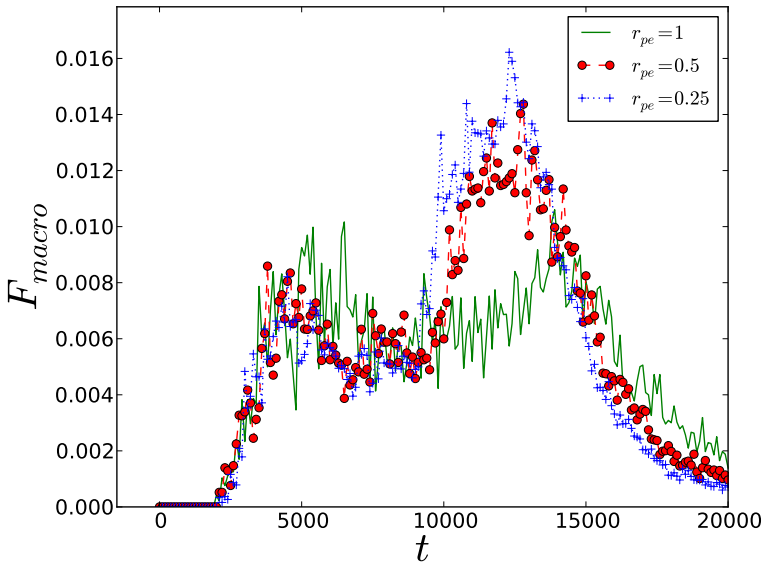

Figure 9: F_{macro} time history when the radius r_{pe} of the particles pe varies.

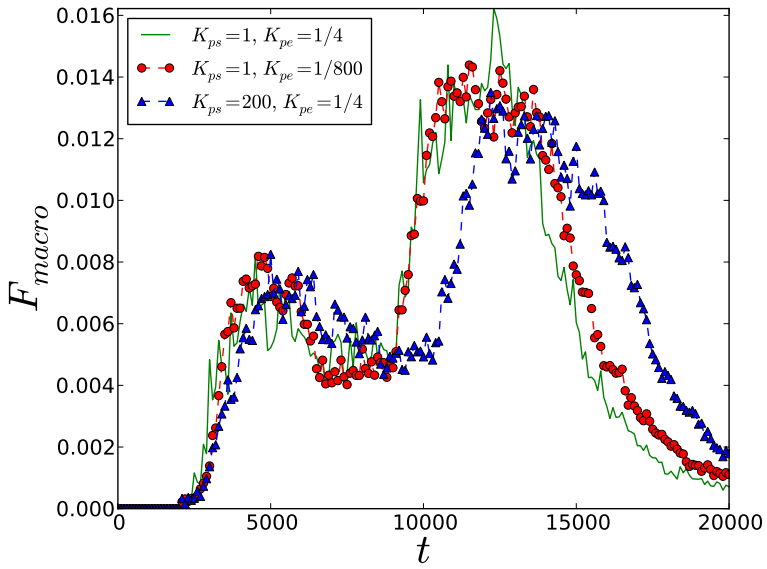

Figure 10: F_{macro} time history when the stiffness K_{pe} and K_{ps} varie.

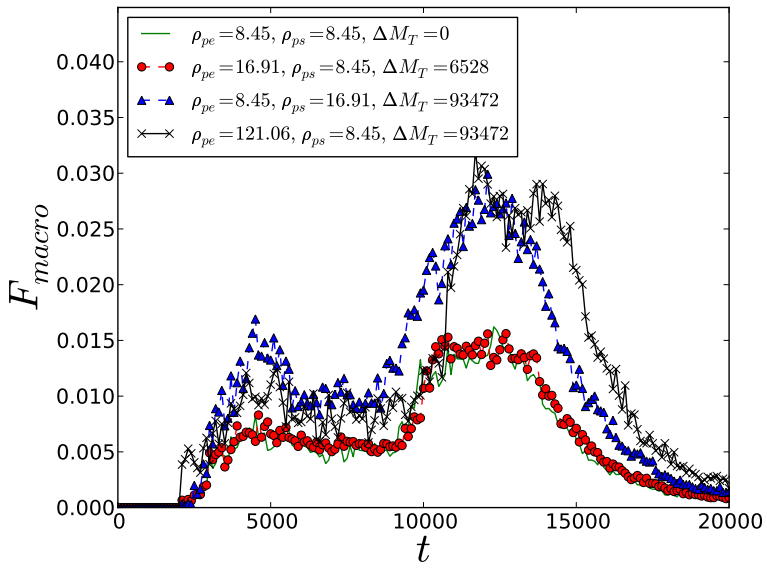

Figure 11: F_{macro} time history when the density ρ_{pe} et ρ_{ps} varie.

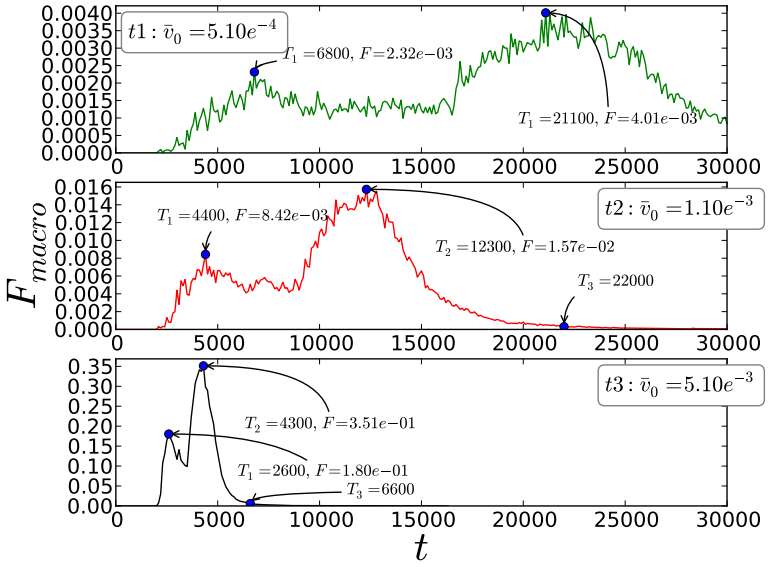

(a)

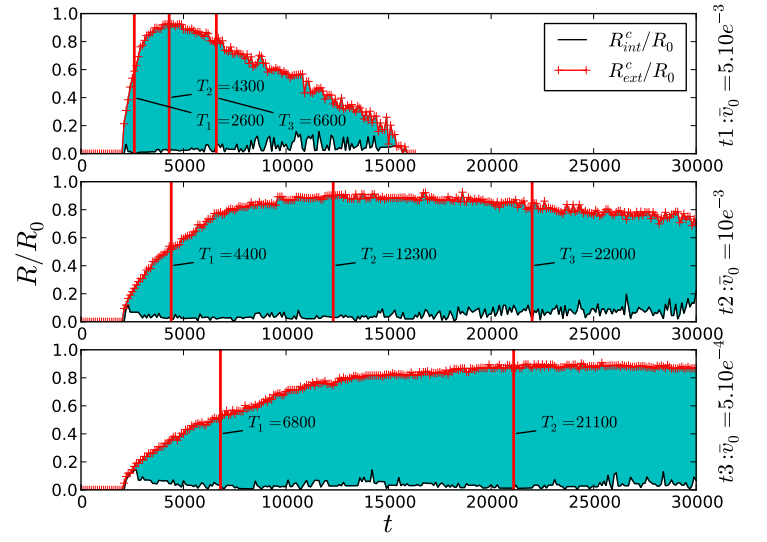

(b)

Figure 12: When the initial speed $\bar{v}_0$ of the impactor varies : a) F_{macro} time history; b) R^c_{ext} and R^c_{int} time history.

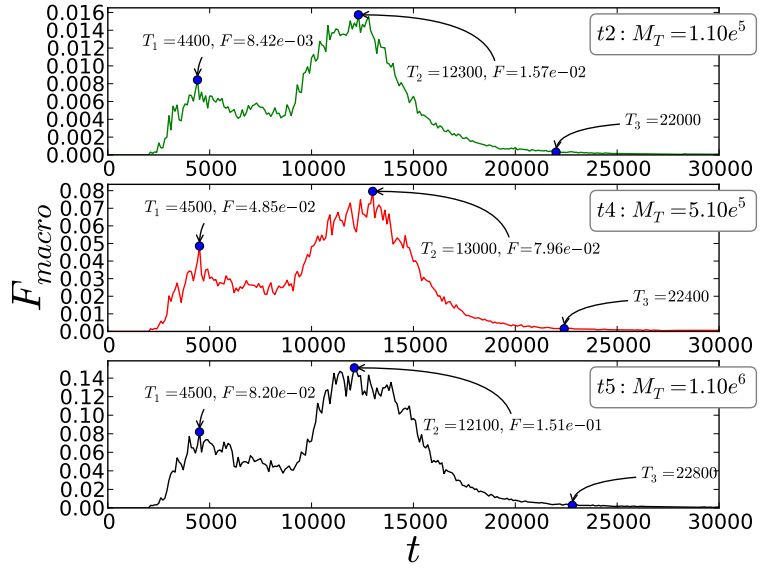

(a)

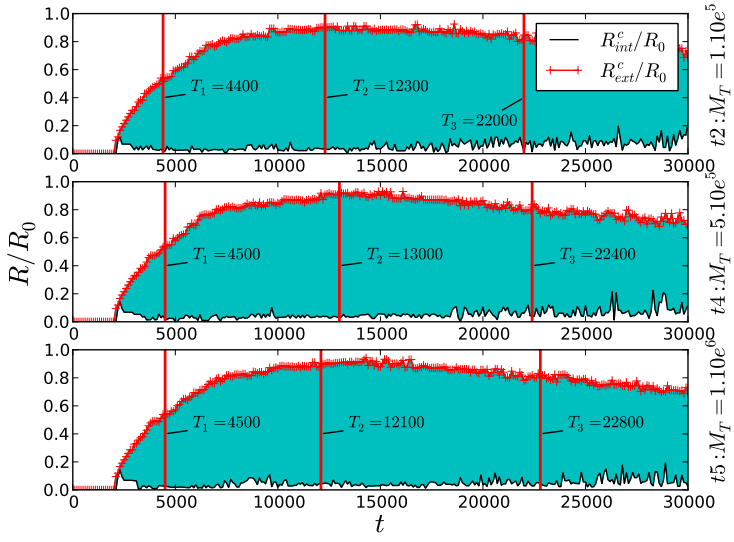

(b)

Figure 13: When the mass M_T of the impactor varies with the density ρ of the particles : a) F_{macro} time history; b) R^c_{ext} and R^c_{int} time history.

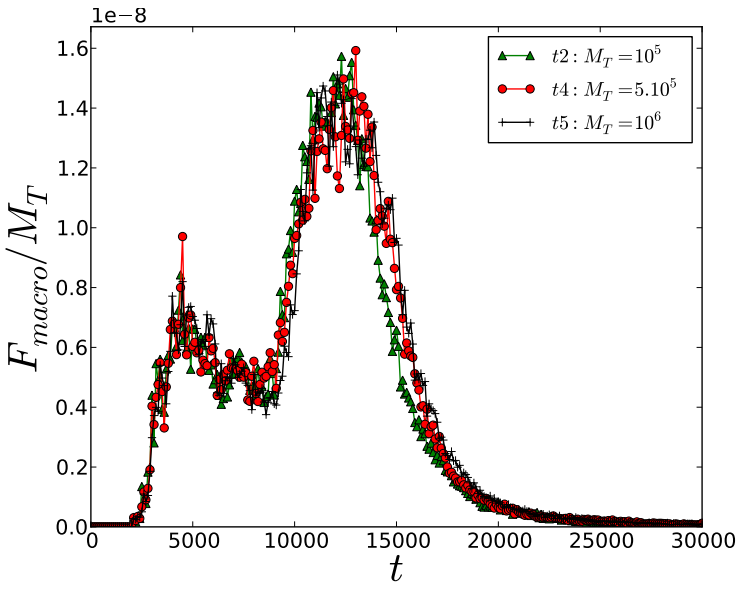

Figure 14: F_{macro}/M_T time history the mass of the impactor M_T varies with the density ρ of the particles.

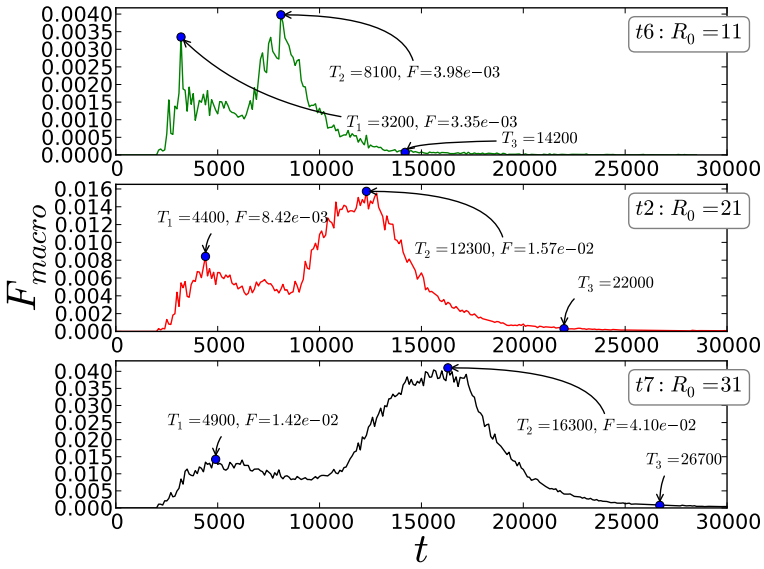

(a)

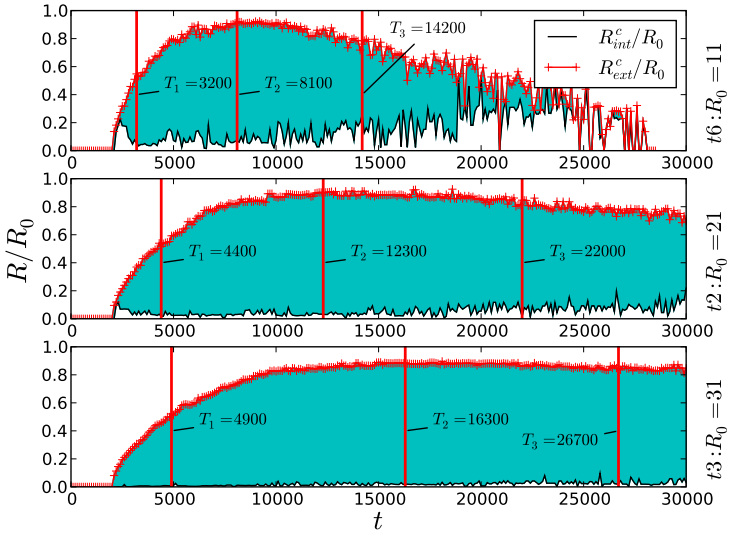

(b)

Figure 15: When the initial radius R_0 of the impactor varies (with $\rho = 8.45$) : a) F_{macro} time history; b) R^c_{ext} and R^c_{int}time history.